

Probing the bright radio flare and afterglow of GRB 130427A with the Arcminute Microkelvin Imager

G. E. Anderson,^{1,2★} A. J. van der Horst,³ T. D. Staley,^{1,2} R. P. Fender,^{1,2}
R. A. M. J. Wijers,³ A. M. M. Scaife,¹ C. Rumsey,⁴ D. J. Titterton,⁴
A. Rowlinson³ and R. D. E. Saunders⁴

¹*School of Physics and Astronomy, University of Southampton, Southampton SO17 1BJ, UK*

²*Department of Physics, Astrophysics, University of Oxford, Denys Wilkinson Building, Oxford OX1 3RH, UK*

³*Astronomical Institute Anton Pannekoek, Science Park 904, PO Box 94249, NL-1090 GE Amsterdam, the Netherlands*

⁴*Astrophysics Group, Cavendish Laboratory, 19 J.J. Thomson Avenue, Cambridge CB3 0HE, UK*

Accepted 2014 March 6. Received 2014 March 5; in original form 2014 February 4

ABSTRACT

We present one of the best sampled early-time light curves of a gamma-ray burst (GRB) at radio wavelengths. Using the Arcminute Microkelvin Imager (AMI), we observed GRB 130427A at the central frequency of 15.7 GHz between 0.36 and 59.32 d post-burst. These results yield one of the earliest radio detections of a GRB and demonstrate a clear rise in flux less than one day after the γ -ray trigger followed by a rapid decline. This early-time radio emission probably originates in the GRB reverse shock so our AMI light curve reveals the first ever confirmed detection of a reverse shock peak in the radio domain. At later times (about 3.2 d post-burst), the rate of decline decreases, indicating that the forward shock component has begun to dominate the light curve. Comparisons of the AMI light curve with modelling conducted by Perley et al. show that the most likely explanation of the early-time 15.7 GHz peak is caused by the self-absorption turn-over frequency, rather than the peak frequency, of the reverse shock moving through the observing bands.

Key words: gamma-ray burst: individual: GRB 130427A – radio continuum: stars.

1 INTRODUCTION

The detection of the early-time multiwavelength radiation from gamma-ray bursts (GRBs) within the first day after the initial flash of γ -rays is essential for refining our understanding of these energetic events. The internal–external shock scenario (Piran 1999) suggests that along with the forward shock, which propagates into the circumburst medium to generate the classical afterglow, there is also emission associated with the reverse shock propagating into the relativistic ejecta (Sari & Piran 1999b). Evidence for the presence of a reverse shock has been demonstrated by the detection of optical flashes (within minutes after the γ -ray trigger) that are not correlated with the initial γ -ray emission from the GRB (Sari & Piran 1999a). Such emission can only be explained by the presence of different physical emitting regions. This same model suggests that the detection of radio flares approximately 1 d post-burst also emanate from the reverse shock (Kulkarni et al. 1999). Such early-time radio signals, which imply a rapid rise and fall in emission within 1 d post-burst, are atypical when compared to the classical radio

afterglow of long GRBs resulting from the forward shock, which slowly evolve on the time-scales of days to years (for a review, see Granot & van der Horst 2014).

The early-time radio signature of GRBs has not been as well investigated as it has in the optical band. This is due to the limited number of large radio telescopes, which are required for such follow-up observations due to the faintness of GRB radio emission. This in turn makes it more difficult to acquire target-of-opportunity observations at the time of the event. Early-time observations have traditionally required human intervention to activate, potentially resulting in the first radio observation of a given GRB being delayed several hours to even days post-burst. As a result, the radio emission emanating from the reverse shock of a GRB has only been observed in a few cases where the earliest radio detections have occurred around 1 d post-burst (e.g., Kulkarni et al. 1999; Frail et al. 2000; Berger et al. 2003).

Only a few robotized, rapid response, follow-up programmes of GRBs have been implemented in the radio domain. For example, attempts were made with the Cambridge Low Frequency Synthesis Telescope at 151 MHz, which triggered on GRBs detected with the Burst And Transient Source Experiment on board the *Compton Gamma-Ray Observatory* (Green et al. 1995; Koranyi et al. 1995;

★E-mail: gemma.anderson@astro.ox.ac.uk

Dessenne et al. 1996). More recently, Bannister et al. (2012) conducted a robotized follow-up experiment using a 12 m radio dish at 1.4 GHz that was specifically designed to search for prompt radio emission associated with GRBs. This telescope triggered on those GRBs detected with the *Swift* γ -ray Burst Mission (Gehrels et al. 2004) and was capable of being on target within a few minutes post-burst. In two out of the nine GRBs observed, a single dispersed radio pulse was possibly detected. In both cases, the candidate's pulse was coincident with breaks in the GRB X-ray light curves.

Over the past two years, a new robotized follow-up programme using the Large Array (LA) interferometer of the Arcminute Microkelvin Imager (AMI; Zwart et al. 2008) has been implemented to obtain immediate observations, and conduct radio monitoring, of *Swift*-detected GRBs at 15.7 GHz. This rapid GRB follow-up programme conducted with AMI is fully automated and is activated when *Swift* triggers on an event, with response times as low as 5 min (Staley et al. 2013). This programme is therefore capable of statistically constraining the radio properties of many *Swift*-detected GRBs (both long and short) within the first hour post-burst, which has never been done before.

One of the most recent radio-bright long GRBs is GRB 130427A, which was detected on 2013 April 27 by both the Gamma-ray Burst Monitor (GBM; Meegan et al. 2009) on board the *Fermi Gamma-ray Space Telescope* at 07:47:06.42 UT (von Kienlin 2013; Zhu et al. 2013) and the Burst Alert Telescope (BAT; Barthelmy et al. 2005) on board the *Swift* GRB mission at 07:47:57 UT (Maselli et al. 2013). GRB 130427A is situated at a redshift of 0.340 making it the closest high-luminosity ($E_{\gamma, \text{iso}} \gtrsim 10^{54}$ erg) GRB since GRB 030329 (Levan et al. 2013a). Such nearby high-energy events are very rare as ~ 80 per cent of *Swift* GRBs are located at $z > 1$ and low-redshift GRBs are often underenergetic (see Perley et al. 2014, and references therein).

The extreme brightness and very early detection of an optical counterpart spurred a rapid succession of multiwavelength follow-up observations making GRB 130427A one of the best spectrally and temporally sampled GRBs to date (Kouveliotou et al. 2013; Laskar et al. 2013; Levan et al. 2013b; Xu et al. 2013; Ackermann et al. 2014; Maselli et al. 2014; Perley et al. 2014). Broad-band modelling conducted by Laskar et al. (2013), Perley et al. (2014), and Panaitescu, Vestrand & Woźniak (2013), using multiwavelength observations ranging from 1 GHz to 0.1 TeV conducted between 300 s and 60 d post-burst, revealed that the emission from GRB 130427A is best described by synchrotron emission from the combination of a reverse and forward shock. Extremely early optical observations conducted with RAPTOR (RAPid Telescopes for Optical Response) also detected a peak in optical emission < 20 s post-burst (Vestrand et al. 2014). This optical flash was temporally coincident with GRB 130427A's prompt γ -ray emission but modelling by Vestrand et al. (2014) demonstrated that it is more likely generated by the GRB's reverse shock. This reverse shock was also shown to dominate the radio and mm wavelength bands from the first hours to days post-burst (Laskar et al. 2013; Panaitescu et al. 2013; Perley et al. 2014).

In this paper, we present AMI observations of the energetic GRB 130427A starting at 0.36 d post-burst, yielding the first early-time (< 1 d) radio detection of a GRB in the Staley et al. (2013) GRB follow-up observing campaign. The observations and data analysis are described in Section 2 with the resulting AMI fluxes and light curve presented in Section 3. In Section 3, we also present a basic broken power-law fit to the AMI light curve of GRB 130427A and discuss how it compares to other early-time radio detections of GRBs. The AMI light-curve modelling is further discussed in Section 4 where we consider the implications of the different slopes,

the position of the peak, and how our results compare to the Very Large Array (VLA) light curves and modelling of GRB 130427A conducted by Perley et al. (2014). In Section 5, we summarize our findings.

2 OBSERVATIONS AND DATA ANALYSIS

GRB 130427A was observed with the AMI LA as part of the robotized GRB follow-up programme described by Staley et al. (2013). The effective frequency range of this telescope is 13.9–17.5 GHz when using frequency channels 3–7, each with a 0.72 GHz bandwidth (channels 1, 2, and 8 are disregarded due to their susceptibility at present to radio interference). AMI LA measures a single linear polarization ($I + Q$) and has a flux root-mean square (rms) noise sensitivity of $3.3 \text{ mJy s}^{-1/2}$ for five frequency channels. The LA consists of eight 12.8 m dishes with baseline lengths between 18–110 m, yielding a primary beam and angular resolution of 5.5 arcmin and ≈ 30 arcsec, respectively, at 15.7 GHz (Zwart et al. 2008). AMI is ideal for the initial follow-up of *Swift* GRBs as its field-of-view fully encompasses the position error of the BAT instrument (1–4 arcsec; Barthelmy et al. 2005). In the follow-up AMI GRB monitoring programme, further observations are then centred on the enhanced *Swift* X-ray Telescope (Burrows et al. 2005) position of the GRB (if X-ray emission is detected), which has a few arcsecond positional accuracy.

AMI was robotically triggered to observe GRB 130427A immediately following the *Swift* trigger. However, as the source was below AMI's horizon, the observation was automatically scheduled for 15:50:35 UT on 2013 April 27, 0.36 d post-burst based on the GBM trigger, when GRB 130427A had reached a sufficient elevation. This first observation was of 1 h duration and took place during wet weather conditions; it was also at the LA's Eastern limit, which resulted in the loss of data due to pointing errors and antenna shadowing. The phase calibrator J1134+2901 was used for this observation, which was found to have a flux of $50.82 \pm 5.09 \text{ mJy}$ in the AMI frequency range. In order to determine how much flux attenuation this first AMI observation suffered due to the low observing altitude and poor weather conditions, we compared the phase calibrator fluxes to those measured by the AMI Small Array (which can be used to calibrate the LA; Franzen et al. 2011) and they agree within 10 per cent. This error is taken into consideration when making flux uncertainty estimates on this data set.

A further 13 AMI observations of GRB 130427A were then manually scheduled between 0.64 and 59.32 d using the phase calibrator J1125+2610, which is $\sim 1 \text{ Jy}$ at 15.7 GHz. These subsequent AMI observations ranged in duration between 1 and 4 h. The first stage of the data reduction involved using the PYTHON script `drive-ami` (the basis of which was originally described in Staley et al. 2013), which analyses all the raw data files belonging to GRB 130427A. This script then runs the most up to date general AMI reduction pipeline, which uses the AMI REDUCE software to automatically flag for interference, shadowing, and hardware errors, performs Fourier transforms of the lag-delay data into frequency channels, and then applies phase and amplitude calibrations (Perrott et al. 2013). The flux calibration was conducted using short observations of 3C286, 3C48, and 3C147. An additional flagging step was also performed on those visibilities for which one (or both) of the involved antennas have 'rain gauge' correction values < 60 per cent of the nominal antenna value. The rain gauge system monitors the system temperature of each antenna to correct for increased noise due to atmospheric disturbances (Zwart et al. 2008). The 60 per cent cutoff is a very

stringent limit that we have applied to the data to specifically target flux attenuation due to rain. This step flagged visibilities in the first April 27 observation as well as in the April 28, May 10, and June 25 observations.

The resulting *uv*-FITS files output by AMI REDUCE were then imported into the Common Astronomy Software Applications package (CASA: Jaeger 2008) for further analysis. Further interactive flagging of radio frequency interference missed by the AMI REDUCE pipeline was performed manually using the CASA task `plotms`. All the individual visibility data sets of GRB 130427A were then imaged with the CASA task `clean` using standard reduction techniques. A single clean box was specified, surrounding the position of GRB 130427A, within which was the only source in the field with a signal-to-noise ratio (SNR) > 3 . The clean threshold was set to ≈ 2 times the rms of the image using a ‘Briggs’ weighting scheme with `Robust` = 0.5.¹ The resulting cleaned images were then imported into MIRIAD (Sault, Teuben & Wright 1995) where the peak flux of the source was measured using the task `imfit`, specifying a point source model. The measured flux error was calculated as the quadratic sum of the image rms and the 5 per cent systematic flux calibration error of AMI (Perrott et al. 2013). This 5 per cent calibration error is conservative as the telescope has been found to be considerably better than this value (for example, see Scaife et al. 2008; Hurley-Walker et al. 2009; Franzen et al. 2011). We assume a more conservative flux calibration error of 10 per cent for the first AMI observation at 0.36 d due to the low observing altitude, poor weather conditions, and the use of a faint phase calibrator (J1134+2901) for this observation. As an additional check, we have measured the flux density of GRB 130427A from each AMI observation, directly from the visibilities, using different levels of automatic and interactive flagging, and splitting individual observations in time. We find that the flux densities measured in this way are fully consistent with the values obtained by imaging.

3 RESULTS

3.1 Identification of the GRB counterpart

In each AMI observation, a single unresolved source was detected, with small deviations in position as expected from the system noise. The absolute position accuracy of the AMI LA has also been studied. For example, in the Tenth Cambridge Survey of radio sources at 15.7 GHz (Franzen et al. 2011), which was conducted with the AMI LA using a ‘rastering’ technique, it was determined that the sources detected with an SNR > 5 have an approximate position error of 3–4 arcsec (Davies et al. 2011). In 7 out of the 10 AMI observations of GRB 130427A where the point source mentioned above had an SNR > 5 , its corresponding MIRIAD `imfit` position was < 4 arcsec from the European VLBI Network position of GRB 130427A (Paragi et al. 2013). The remaining three were within 6.6 arcsec of the VLBI position. For each of the 14 AMI observations, we calculated the Right ascension (RA) and declination (Dec.) rms position error resulting from the MIRIAD `imfit` of this source using equations 4a, 4b, and 5 from Perrott et al. (2013). In all but one AMI observation, the offset between the MIRIAD `imfit` and VLBI position was less than three times the quadratic sum of the RA and Dec. rms errors. However, as the MIRIAD `imfit` position of the remaining detection of the source is < 4 arcsec from the majority of the other AMI detections, it is extremely likely that it is the same

¹ See Dan Briggs’ PhD thesis <http://www.aoc.nrao.edu/dissertations/dbriggs/>.

Table 1. AMI Observations of GRB 130427A.

Obs. time ^a (UT)	Days since burst ^b	Flux density ^c (mJy)
2013/04/27.68	0.36	3.44 ± 0.38
2013/04/27.96	0.64	4.16 ± 0.22
2013/04/28.88	1.55	1.64 ± 0.13
2013/04/29.80	2.48	1.03 ± 0.09
2013/04/29.97	2.65	0.94 ± 0.09
2013/04/30.88	3.55	0.61 ± 0.06
2013/05/01.91	4.58	0.56 ± 0.05
2013/05/02.85	5.53	0.51 ± 0.06
2013/05/04.85	7.52	0.45 ± 0.05
2013/05/07.97	10.64	0.35 ± 0.05
2013/05/10.90	13.58	0.31 ± 0.07
2013/05/21.77	24.44	0.28 ± 0.05
2013/06/05.77	39.44	0.23 ± 0.05
2013/06/25.65	59.32	0.12 ± 0.04

^aThe date of the observation corresponds to the mid-point of the AMI integration.

^bThe days since burst are relative to the initial *Fermi* GBM detection of GRB 130427A.

^cThe flux error is the quadratic sum of the image’s rms and the 5 per cent systematic flux calibration error with the exception of the observation at 2013/04/27.68, which assumes a conservative 10 per cent calibration error (see Section 2).

source in all 14 AMI observations. We therefore identify this source as the radio afterglow of GRB 130427A.

The final results for each AMI observation of GRB 130427A are listed in Table 1. This table includes the observing time of each AMI observation, the number of days the observation took place after the *Fermi* GBM trigger, and the flux measured with MIRIAD `imfit`.

3.2 Historical context and brightness temperature

Historically, the earliest radio detections of GRBs in the literature occur approximately 1 d post-burst. For example, Kulkarni et al. (1999) detected a short-lived radio flare from GRB 990123 peaking at ~ 1.24 d post-burst. Rigorous radio observations both before and after this single detection only yielded upper limits, which lead to Kulkarni et al. (1999) interpreting this brief radio counterpart appearance as emission from the GRB’s reverse shock. Consequently, similar observations were also conducted for GRB 991216 (Frail et al. 2000) and GRB 020405 (Berger et al. 2003). In both cases, early radio observations took place ≈ 1 d post-burst, resulting in the detection of a radio counterpart. These counterparts then rapidly faded but were still detectable several weeks post-burst. This rapid decrease in radio flux is atypical when compared to the rise and decay of most radio afterglows that result from the forward shock, which tend to peak between 3 and 100 d post-burst (Chandra & Frail 2012). The reverse shock was therefore the most likely interpretation for the early-time radio emission observed from GRB 991216 and GRB 020405 (see Frail et al. 2000; Berger et al. 2003, respectively).

The early-time AMI detection of GRB 130427A at 0.36 d is one of the earliest detections of a long GRB at radio wavelengths [long GRBs that have earlier radio detections with significance $> 3\sigma$ include GRB 010222 (Frail et al. 2002), GRB 130215A (Perley & Keating 2013), GRB 130418A (Perley 2013), and GRB 130907A (Corsi 2013)]. If we assume that the emission from GRB 130427A

Table 2. Brightness temperatures and minimum Lorentz factors calculated for GRBs with early-time radio detections.

GRB	Redshift	Luminosity distance ^a (Gpc)	Frequency (GHz)	Days since burst	Brightness temperature ($\times 10^{15}$ K)	Minimum Lorentz factor Γ	Reference ^b
990123	1.6	11.7	8.46	1.24	1.9	12.3	1
991216	1.02	6.7	15.0	1.33	0.9	9.7	2
991216	1.02	6.7	8.46	1.49	2.0	12.6	2
010222	1.477	10.6	22.5	0.32	9.2	21.0	3
010222	1.477	10.6	350.0	0.35	0.2	5.8	4
020405	0.69	4.1	8.46	1.19	0.7	8.9	5
130215A	0.597	3.5	93.0	0.11	3.1	14.6	6
130418A	1.218	8.4	93.0	0.34	1.4	11.2	7
130427A	0.340	1.8	15.7	0.36	3.7	15.4	8
130427A	0.340	1.8	5.1	0.68	3.6	15.4	9, 10
130907A	1.238	8.5	24.5	0.17	33.2	32.1	11

^aThe luminosity distance was calculated from the redshift using the online cosmology calculator developed by Wright (2006) assuming cosmological parameters $H_0 = 72 \text{ km s}^{-1} \text{ Mpc}^{-1}$, $\Omega_M = 0.27$, and $\Omega_{\text{vac}} = 0.73$.

^bReferences for the radio detection used to calculate the brightness temperature for each GRB. 1: Kulkarni et al. (1999); 2: Frail et al. (2000); 3: Frail et al. (2003); 4: Frail et al. (2002); 5: Berger et al. (2003); 6: Perley & Keating (2013); 7: Perley (2013); 8: This paper; 9: Laskar et al. (2013); 10: Perley et al. (2014); 11: Corsi (2013).

is a non-relativistic flow that emanates from a region of size ct , then a brightness temperature of $T_b = 3.7 \times 10^{15} \text{ K}$ is calculated from the first AMI observation using

$$T_b = 1.153 \times 10^{-8} d^2 F_\nu \nu^{-2} t^{-2} (1+z)^{-1}, \quad (1)$$

where d is the distance to the GRB in cm, F_ν the flux in Jy, ν is the observing frequency in Hz, t is time in seconds since the γ -ray trigger, and z the redshift (Longair 2011). Since ct is the maximum size of the emitting region, and the maximum brightness temperature is the inverse-Compton limit $T_b \approx 10^{12} \text{ K}$, then one derives a minimum Lorentz factor from the observed brightness temperature such that $T_b/T_b = \Gamma^3$ (Galama et al. 1999). The minimum bulk Lorentz factor predicted by the earliest AMI observation of GRB 130427A is therefore $\Gamma \gtrsim 15.4$, confirming its relativistic nature.

A comparison between the brightness temperature calculated from this first AMI observation of GRB 130427A and those calculated from the $\approx 1 \text{ d}$ radio detections of the confirmed reverse-shock-detected GRBs (GRB 990123, GRB 991216, and GRB 020405), the four early-time ($< 0.36 \text{ d}$ post burst) radio-detected GRBs mentioned above (GRB 010222, GRB 130215A, GRB 130418A, and GRB 130907A), and the earliest VLA detection of GRB 130427A, can be found in Table 2. This table lists the redshift of the GRB and its corresponding luminosity distance in Gpc calculated using Wright (2006), the frequency of the observation, the time of detection in days post-burst, the brightness temperature calculated using equation (1), and the corresponding predicted minimum Lorentz factor. These results demonstrate that our early AMI observation of GRB 130427A represents one of the highest brightness temperatures and Lorentz factors based on radio observations. The AMI GRB robotic follow-up programme therefore has the potential to play an important role in increasing this sample significantly.

3.3 Description and fit to the light curve

The peak in the AMI light curve of GRB 130427A around 1 d post-burst is a signature that has never been observed from a GRB at such early times in the radio frequency domain. Investigations by Perley et al. (2014) determined that the transition frequency between weak and strong scattering at the Galactic latitude of GRB 130427A is about 5 GHz, which places the AMI observing frequency in the

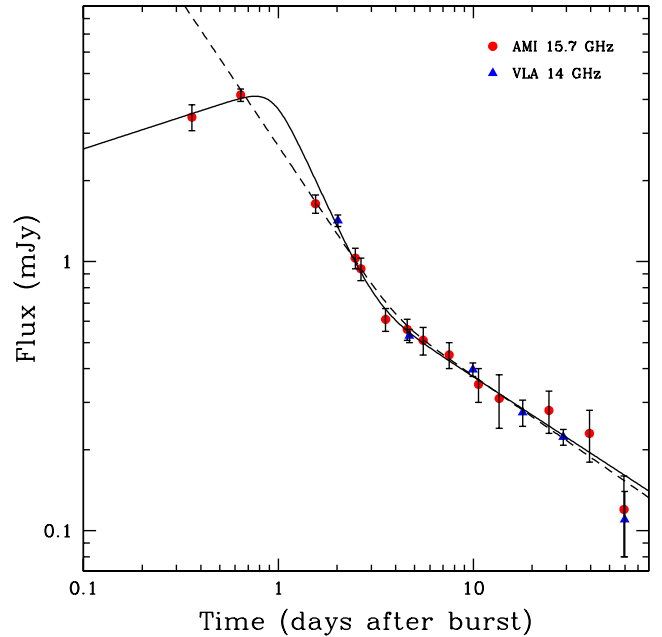


Figure 1. The AMI 15.7 GHz light curve of GRB 130427A (red circles). Overplotted are the VLA detections of GRB 130427A at 14 GHz (blue triangles). The solid line is the double broken power-law fit to all the AMI and VLA data points. The dashed line is the single broken power law, which is a fit to all but the first data point. All errors are 1σ .

weak-scattering regime where the modulation index is only a few per cent; scintillation is therefore unlikely to be the cause of the peak feature in the AMI light curve. Fig. 1 shows the AMI light curve of GRB 130427A (red circles), which is better sampled than the VLA 13–16 GHz observations (blue triangles).

The afterglow from a GRB is generally well described by a decaying single or broken power law resulting from the relativistic ejecta decelerating as it sweeps up the ambient medium (Sari, Piran & Narayan 1998; Sari, Piran & Halpern 1999). In order to quantify the behaviour of the GRB 130427A AMI light curve, we fit two different broken power laws to the data. The initial broken power-law

fit ignores the first AMI data point, concentrating on the decaying part of the light curve. This fit results in a break time at 4.0 d with a pre-break temporal decay slope of $\alpha = -1.1$ and a post-break slope of $\alpha = -0.5$ ($\chi^2_{\text{red}} = 1.09$) for $F(t) \propto t^\alpha$. This power-law fit is shown as a dashed line in Fig. 1. Clearly this broken power law does not describe the early-time emission from GRB 130427A that we have observed with AMI as it predicts a 15.7 GHz flux of around 8 mJy at 0.36 d post-burst. This fit overestimates the measured AMI flux at 0.36 d by a factor of 2.4, which is equivalent to 13 standard deviations. As explained in Section 2, this is well outside the flux attenuation that we might expect to have occurred during this observation. We therefore confirm that the increase in 15.7 GHz flux <0.64 d post-burst is a real feature.

We next fit a double broken power law to all the data points in the AMI light curve. This fit resulted in a temporal power-law rise of $\alpha = 0.2$, peaking at 0.9 d, followed by two temporal decay slopes of $\alpha = -1.6$ and -0.5 with a break time at 3.2 d ($\chi^2_{\text{red}} = 1.06$). This double broken power-law fit is depicted as a solid line in Fig. 1. The earlier decay index is comparable to those calculated from power-law fits to the early-time (<10 d post-burst) radio detections of GRB 991216 ($\alpha_d = -0.82 \pm 0.02$; Frail et al. 2000) and GRB 020405 ($\alpha_d = -1.2 \pm 0.4$; Berger et al. 2003). The AMI light curve of GRB 130427A is also clearly declining at ~ 1 d post-burst, which is consistent with the radio light curves of GRB 990123, GRB 991216, and GRB 020405, and therefore with a reverse shock interpretation.

4 INTERPRETATION

Broad-band spectral modelling of GRB 130427A, which utilizes observations from GHz radio wavelengths to GeV γ -ray energies, has revealed that the GRB afterglow emission is best described by a two-component synchrotron shock model, which is highly suggestive of the standard forward/reverse shock interpretation (Laskar et al. 2013; Panaitescu et al. 2013; Maselli et al. 2014; Perley et al. 2014). In this picture, the forward shock causes the emission at optical and X-ray frequencies after 0.1 d and the radio emission after a few weeks, while the earlier emission at those frequencies is dominated by the reverse shock. Emission from the forward shock may also extend into the high-energy γ -ray regime, but this requires changes in the models of particle acceleration up to these very high energies (Kouveliotou et al. 2013; Ackermann et al. 2014).

The earliest VLA observations began ~ 0.68 d post-burst and yielded detections at 5.1 and 6.8 GHz (Laskar et al. 2013; Perley et al. 2014). The 5 GHz VLA light curve also indicates a peak, but at ~ 2 d, and the very well-sampled light curve at this frequency taken with the Westerbork Synthesis Radio Telescope (WSRT) shows that this peak occurs at around 1.6 d post-burst (van der Horst et al., in preparation). If the peak at 5 GHz is real then comparing this light curve with the AMI 15.7 GHz light curve of GRB 130427A shows the progression of the peak of the reverse shock occurring at later times with decreasing frequency, which is expected as a generic feature of all synchrotron models (e.g. van der Laan 1966). However, based on the VLA observations alone it is not possible to rule out interstellar scintillation as the cause of the 5 GHz peak since the source size at this time is small enough for scintillation effects to still be influencing the observed flux (Perley et al. 2014).

The earliest VLA observations at 5.1 and 6.8 GHz, 0.68 d post-burst, suggest that the spectrum of GRB 130427A may have been affected by synchrotron self-absorption at this time. This is demonstrated by the steep spectral index $\beta \approx 2.4$ (for $S_\nu \propto \nu^\beta$) between

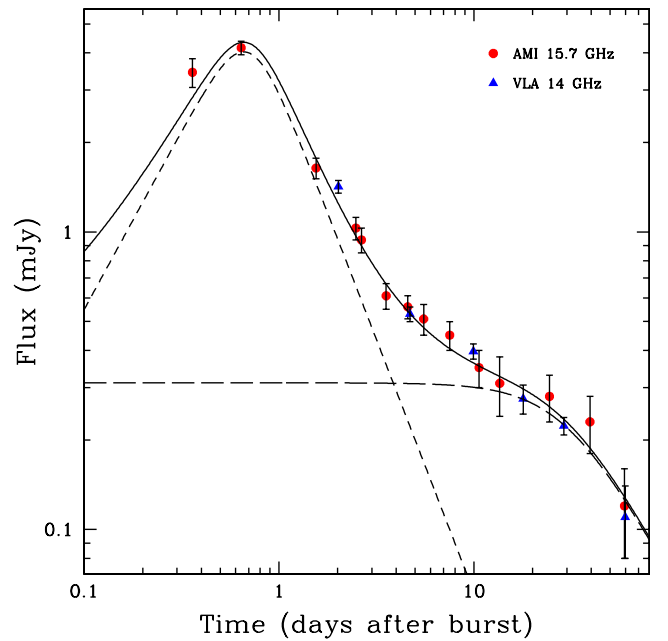


Figure 2. The AMI 15.7 GHz and VLA 14 GHz light curve of GRB 130427A overplotted with the afterglow model derived by Perley et al. (2014, solid line) showing the individual contributions from the reverse shock (short dashed line) and forward shock (long dashed line). The AMI peak at ~ 0.7 d is one of the earliest radio peaks ever observed from a GRB.

these two frequencies. These VLA observations coincide with the 15.7 GHz flux peak seen in the second AMI observation at 0.64 d. A comparison between the VLA and AMI fluxes demonstrate that the spectrum was indeed increasing with frequency at that time between 5.1 and 15.7 GHz ($\beta \approx 1$), although not as steeply as between 5.1 and 6.8 GHz. This indicates that the peak of the spectral energy distribution of GRB 130427A was close to 15.7 GHz around ~ 0.7 d post-burst, which is also confirmed by the peak observed in the 15.7 GHz light curve. The early radio peak in the AMI light curve is therefore caused by the synchrotron self-absorption turn-over frequency (ν_a) moving through the observing bands rather than by the peak frequency (ν_m ; for details regarding the GRB characteristic frequencies, see Sari & Piran 1999b).

The double broken power-law fit to the AMI data in Fig. 1 shows a dramatic slow-down in the power-law decay of the light curve at 3.2 d post-burst. Such a change in the power-law index is atypical when compared to the power-law breaks seen from GRBs at shorter wavelengths, which instead steepen due to the slowing of their collimated (jet) outflows (Sari et al. 1999). This flattening in the light-curve decay suggests the presence of a second spectral component that is beginning to rise at late times in the radio band. This second component is interpreted by Perley et al. (2014) as the forward shock beginning to dominate over the reverse shock emission. In Fig. 2, we show a model light curve comprised of a reverse shock and a forward shock component. Note that this is not a formal fit to the 15.7 GHz light curve, which is in fact not possible given the large number of free parameters compared to the number of light-curve data points, but is instead based on the fit results presented by Perley et al. (2014), which assumes ν_a is causing the reverse shock peak.

Perley et al. (2014) argue that the radio-to-X-ray broad-band spectra show that the jet from GRB 130427A is moving through a medium structured like a stellar wind that has an electron energy

index of $p \simeq 2.14$. Perley et al. (2014) also use the resulting light-curve slopes to calculate that the reverse shock is Newtonian (often described as the thin-shell case) in which the shock does not become relativistic while crossing the shell behind the forward shock. In this scenario the Lorentz factor of the shock depends on the radius as $\Gamma \propto r^{-g}$ (Kobayashi & Sari 2000), and therefore the light-curve slopes depend on the free parameter g , which is specific to this model. The theoretical range of allowed g values is $1/2 < g < 3/2$ in the case of a stellar wind medium (see Zou, Wu & Dai 2005). Since we have shown based on the AMI and VLA observations between 0.64–0.68 d that the peak of the 15.7 GHz light curve is caused by the passage of v_a , the theoretical pre-peak slope is $(25g + 40)/(28g + 14)$ and the post-peak slope is $-((15g + 24)p + 7g)/(28g + 14)$ (Zou et al. 2005). In Perley et al. (2014), it is shown that the broad-band light curves are best fitted with $g \simeq 3$, resulting in pre-peak and post-peak slopes of 1.2 and -1.7 , respectively (see Fig. 2). We have adopted this value for g even though it is outside of the theoretically allowed range (as also pointed out by Laskar et al. 2013; Panaitescu et al. 2013). The maximum allowed value of $g \simeq 3/2$ results in too steep light-curve slopes of 1.4 and -2.0 . We note, however, that these theoretical light-curve slopes have been derived assuming that we are observing straight into the jet. A viewing angle away from the jet axis but smaller than the jet opening angle could remedy this discrepancy.

For the model curves shown in Fig. 2, it is clear that the forward shock is contributing to the total flux at all times, but starts to dominate the 15.7 GHz emission after 3 d. Perley et al. (2014) have shown that v_a of the forward shock is below this observing band. The turn-over in the light curve, which Perley et al. (2014) calculated to be at ~ 30 d, is therefore caused by v_m passing through, when the forward shock post-peak light-curve slope changes from 0 to $-(3p - 1)/4 \simeq -1.4$ (Meszaros, Rees & Wijers 1998).

5 CONCLUSIONS

The AMI light curve of GRB 130427A agrees well with the forward/reverse shock interpretation suggested by many authors such as Perley et al. (2014), Panaitescu et al. (2013), and Laskar et al. (2013). These early-time AMI observations (within one day post-burst) have enabled us to not only obtain one of the earliest detections of a long GRB, but also capture the peak in the reverse shock emission at 15.7 GHz. This result has allowed us to further constrain the possible models of the early-time afterglow from GRB 130427A by demonstrating that v_a , rather than v_m , is the cause of the radio light-curve peak. This scenario will be further investigated by combining the AMI and VLA light curves with fine time sampling observations obtained with the WSRT in van der Horst et al. (in preparation).

The detection of the reverse shock radio peak in the AMI light curve of GRB 130427A clearly demonstrates the importance of rapid response radio follow-up programmes of GRBs. The AMI GRB follow-up programme (Staley et al. 2013) is therefore crucial for exploring the early-time radio signatures of GRBs and constraining the radio properties of these events within the first few hours post-burst.

ACKNOWLEDGEMENTS

We thank the staff of the Mullard Radio Astronomy Observatory for their invaluable assistance in the operation of AMI. Special thanks also goes to Natasha Hurley-Walker, Guy Pooley, and Yvette

Perrott for their advice and help with this research and to the referee for their constructive response and suggestions. GEA, TDS, RPF acknowledge the support of the European Research Council Advanced Grant 267697 ‘4 Pi Sky: Extreme Astrophysics with Revolutionary Radio Telescopes’. AJvdH, RAMJW and AR acknowledge support from the European Research Council via Advanced Investigator Grant no. 247295. CR acknowledges the support of an STFC studentship.

REFERENCES

- Ackermann M. et al., 2014, *Science*, 343, 42
 Bannister K. W., Murphy T., Gaensler B. M., Reynolds J. E., 2012, *ApJ*, 757, 38
 Barthelmy S. D. et al., 2005, *Space Sci. Rev.*, 120, 143
 Berger E., Soderberg A. M., Frail D. A., Kulkarni S. R., 2003, *ApJ*, 587, L5
 Burrows D. N. et al., 2005, *Space Sci. Rev.*, 120, 165
 Chandra P., Frail D. A., 2012, *ApJ*, 746, 156
 Corsi A., 2013, *GCN Circ.*, 15200
 Davies M. L. et al., 2011, *MNRAS*, 415, 2708
 Dessenne C. A.-C. et al., 1996, *MNRAS*, 281, 977
 Frail D. A. et al., 2000, *ApJ*, 538, L129
 Frail D. A. et al., 2002, *ApJ*, 565, 829
 Frail D. A., Kulkarni S. R., Berger E., Wieringa M. H., 2003, *AJ*, 125, 2299
 Franzen T. M. O. et al., 2011, *MNRAS*, 415, 2699
 Galama T. J. et al., 1999, *Nature*, 398, 394
 Gehrels N. et al., 2004, *ApJ*, 611, 1005
 Granot J., van der Horst A. J., 2014, *PASA*, in press
 Green D. A. et al., 1995, *Ap&SS*, 231, 281
 Hurley-Walker N. et al., 2009, *MNRAS*, 396, 365
 Jaeger S., 2008, in Argyle R. W., Bunclark P. S., Lewis J. R., eds, *ASP Conf. Ser. Vol. 394, Astronomical Data Analysis Software and Systems XVII*. Astron. Soc. Pac., San Francisco, p. 623
 Kobayashi S., Sari R., 2000, *ApJ*, 542, 819
 Koranyi D. M., Green D. A., Warner P. J., Waldrum E. M., Palmer D. M., 1995, *MNRAS*, 276, L13
 Kouveliotou C. et al., 2013, *ApJ*, 779, L1
 Kulkarni S. R. et al., 1999, *ApJ*, 522, L97
 Laskar T. et al., 2013, *ApJ*, 776, 119
 Levan A. J., Cenko S. B., Perley D. A., Tanvir N. R., 2013a, *GCN Circ.*, 14455
 Levan A. J. et al., 2013b, preprint ([arXiv:astro-ph/1307.5338](https://arxiv.org/abs/1307.5338))
 Longair M. S., 2011, *High Energy Astrophysics*, 3rd edn., Cambridge Univ. Press, Cambridge
 Maselli A., Beardmore A. P., Lien A. Y., Mangano V., Mountford C. J., Page K. L., Palmer D. M., Siegel M. H., 2013, *GCN Circ.*, 14448
 Maselli A. et al., 2014, *Science*, 343, 48
 Meegan C. et al., 2009, *ApJ*, 702, 791
 Meszaros P., Rees M. J., Wijers R. A. M. J., 1998, *ApJ*, 499, 301
 Panaitescu A., Vestrand W. T., Woźniak P., 2013, *MNRAS*, 436, 3106
 Paragi Z., van der Horst A. J., Yang J., Kouveliotou C., Wijers R. A. M. J., Granot J., 2013, *Astron. Telegram*, 5242
 Perley D. A., 2013, *GCN Circ.*, 14387
 Perley D. A., Keating G., 2013, *GCN Circ.*, 14210
 Perley D. A. et al., 2014, *ApJ*, 781, 37
 Perrott Y. C. et al., 2013, *MNRAS*, 429, 3330
 Piran T., 1999, *Phys. Rep.*, 314, 575
 Sari R., Piran T., 1999a, *ApJ*, 517, L109
 Sari R., Piran T., 1999b, *ApJ*, 520, 641
 Sari R., Piran T., Narayan R., 1998, *ApJ*, 497, L17
 Sari R., Piran T., Halpern J. P., 1999, *ApJ*, 519, L17
 Sault R. J., Teuben P. J., Wright M. C. H., 1995, in Shaw R. A., Payne H. E., Hayes J. J. E., eds, *ASP Conf. Ser. Vol. 77*, *Astronomical Data Analysis Software and Systems IV*. Astron. Soc. Pac., San Francisco, p. 433

Scaife A. M. M. et al., 2008, MNRAS, 385, 809
Staley T. D. et al., 2013, MNRAS, 428, 3114
van der Laan H., 1966, Nature, 211, 1131
Vestrand W. T. et al., 2014, Science, 343, 38
von Kienlin A., 2013, GCN Circ., 14473
Wright E. L., 2006, PASP, 118, 1711
Xu D. et al., 2013, ApJ, 776, 98

Zhu S., Racusin J., Kocevski D., McEnery J., Longo F., Chiang J., Vianello G., 2013, GCN Circ., 14471
Zou Y. C., Wu X. F., Dai Z. G., 2005, MNRAS, 363, 93
Zwart J. T. L. et al., 2008, MNRAS, 391, 1545

This paper has been typeset from a $\mathrm{T}_{\mathrm{E}}\mathrm{X}/\mathrm{L}^{\mathrm{A}}\mathrm{T}_{\mathrm{E}}\mathrm{X}$ file prepared by the author.